Increasing fault slip rates within the Corinth Rift, Greece: A rapidly localising active rift fault network

Casey W. Nixon [a,*], Lisa C. McNeill [b], Robert L. Gawthorpe [a], Donna J. Shillington [c], Georgios Michas [d], Rebecca E. Bell [e], Aaron Moyle [b], Mary Ford [f], Natalia V. Zakharova [g], Jonathan M. Bull [b], Gino de Gelder [h]

[a] Department of Earth Science, University of Bergen, Bergen, Norway
[b] Ocean and Earth Science, National Oceanography Centre Southampton, University of Southampton, European Way, Southampton, United Kingdom
[c] School of Earth and Sustainability, Northern Arizona University, Flagstaff, AZ, USA
[d] Department of Geology and Geoenvironment, National and Kapodistrian University of Athens, Athens, Greece
[e] Department of Earth Science and Engineering, Imperial College, London, United Kingdom
[f] Université de Lorraine, CNRS, CRPG, Nancy, France
[g] Department of Earth and Atmospheric Sciences, Central Michigan University, Mt Pleasant, Michigan, USA
[h] ISTerre, CNRS, Université Grenoble Alpes, Saint Martin d'Hères, France

ARTICLE INFO

ABSTRACT

As a young (<5 Myr old) active rift with high resolution spatial and temporal constraints, the Corinth Rift is a natural laboratory for testing models of rift and fault network development in the early stages of continental rifting. New analyses of the rift fault network in the offshore syn-rift sequence are combined with ocean drilling borehole data from IODP Expedition 381. The expedition drilled and sampled syn-rift sediments from the last few Myr and provides the first absolute age framework for the offshore rift, allowing determination of robust fault slip rates and temporal patterns in fault network activity.

Spatial variations in activity and rates throughout the rift fault network, for four time intervals over the past ~2 Myr, illustrate changes in strain distribution and highlight three dominant processes controlling the development of the fault network: 1) progressive strain localisation and transfer of strain from major S-dipping to major N-dipping faults from ~2 Ma – 130 ka; 2) linkage of a southern border fault system and subsequent acceleration of fault slip rates on major N-dipping faults at ~335 ka; 3) increased rift margin flexure and subsequent deformation since ~130 ka, a response to rapid subsidence in the hanging wall of an established crustal scale border fault system.

Since ~130 ka the rift fault network has experienced a two-fold increase in average cumulative slip rates, with the highest slip rates (>7 mm/yr) occurring on major segments of the border fault system in the central rift. A comparison of seismic moment rates from historical earthquakes (last 320 years) is consistent with the geological timescale of fault slip rates (highest rates in the western and central rift), but not with the distribution of very recent activity (from 50-year earthquake records). As a result, a moment deficit is present along the central rift, which could be accommodated by a large (Mw 6.5) earthquake, potentially even rupturing multiple linked fault segments.

The details of rift fault network activity from this study reveal how quickly strain can migrate and become localised during early continental rifting, and how rapidly fault slip accelerates in response to the establishment of major rift border fault systems. Identifying the nature and timescales of these important rift processes furthers our models of early rift evolution and has implications for assessing seismic hazard in regions of active continental rifting.

* Corresponding author.
  E-mail address: casey.nixon@uib.no (C.W. Nixon).

1. Introduction

The establishment of fault networks in the early stages of continental rifting exerts a fundamental control on rift evolution and architecture, dictating the distribution of extensional strain and the potential transition into seafloor spreading (e.g., Bell et al., 2009; Bosworth et al., 2005; Gawthorpe et al., 2003; Whitmarsh et al., 2001). Studies of syn-rift deformation at mature rifts and passive margins highlight that rift fault networks often evolve from a distributed array of faults to a population where strain is localised onto a few large, fast moving and well-connected fault systems (e.g., Cowie et al., 2005; Gawthorpe et al., 2003; Nicol et al., 1997; Walsh et al., 2003). This process of strain localisation results in the formation of border fault systems that accumulate kilometres of slip. Border fault systems control basin geometries and sedimentary routing systems (Bosworth et al., 2005; Pechlivanidou et al., 2019; Sharp et al., 2000), whilst their growth and linkage impact depocentre development (e.g., Morley, 1999; Nixon et al., 2016) and represent significant earthquake hazard (e.g., Bernard et al., 2006; Jackson et al., 1982).

For many studies, the finest achievable rift-scale temporal resolution is of the order of ≥1 Myr, meaning the details of rift fault network evolution are missed. Moreover, observations of the first few million years of rifting are rare or obscured due to poor geochronology, erosion/

deep-burial of earlier syn-rift sediments, or tectonic overprinting. Within active rift systems some studies have managed to investigate fault activity at higher temporal resolutions (<1 Myr), however these often focus on the most recent activity only (e.g., Morley et al., 2000; Nixon et al., 2014) or are confined to a single fault system (e.g., Hemelsdaël and Ford, 2014; Taylor et al., 2004) or miss the first few million years of rifting (e.g., McCartney and Scholz, 2016). This paucity of data means that fault slip rates, variations in fault network activity and how strain is accommodated and distributed throughout a rift in time and space during early continental rifting remain poorly resolved.

In this contribution we revisit the young, <5-Myr-old, active Corinth Rift, central Greece (Fig. 1A), which is one of Europe's most seismically-energetic areas. The rift has been the focus of rapid N-S extension within the Aegean since the Pliocene-early Pleistocene (Leeder et al., 2008; Ori, 1989), with active rifting focused in the Gulf of Corinth initiating ~2 Ma (Leeder et al., 2008; McNeill et al., 2005b) and exhibiting geodetic extension rates up to 15–20 mm/yr (Avallone et al., 2004; Bernard et al., 2006; Briole et al., 2000; Clarke et al., 1998). These high extension rates combined with high sediment fluxes (McNeill et al., 2019b; Nixon et al., 2016; Watkins et al., 2018) and a well-preserved syn-rift record make the Corinth Rift an ideal natural laboratory for studying early continental rifting.

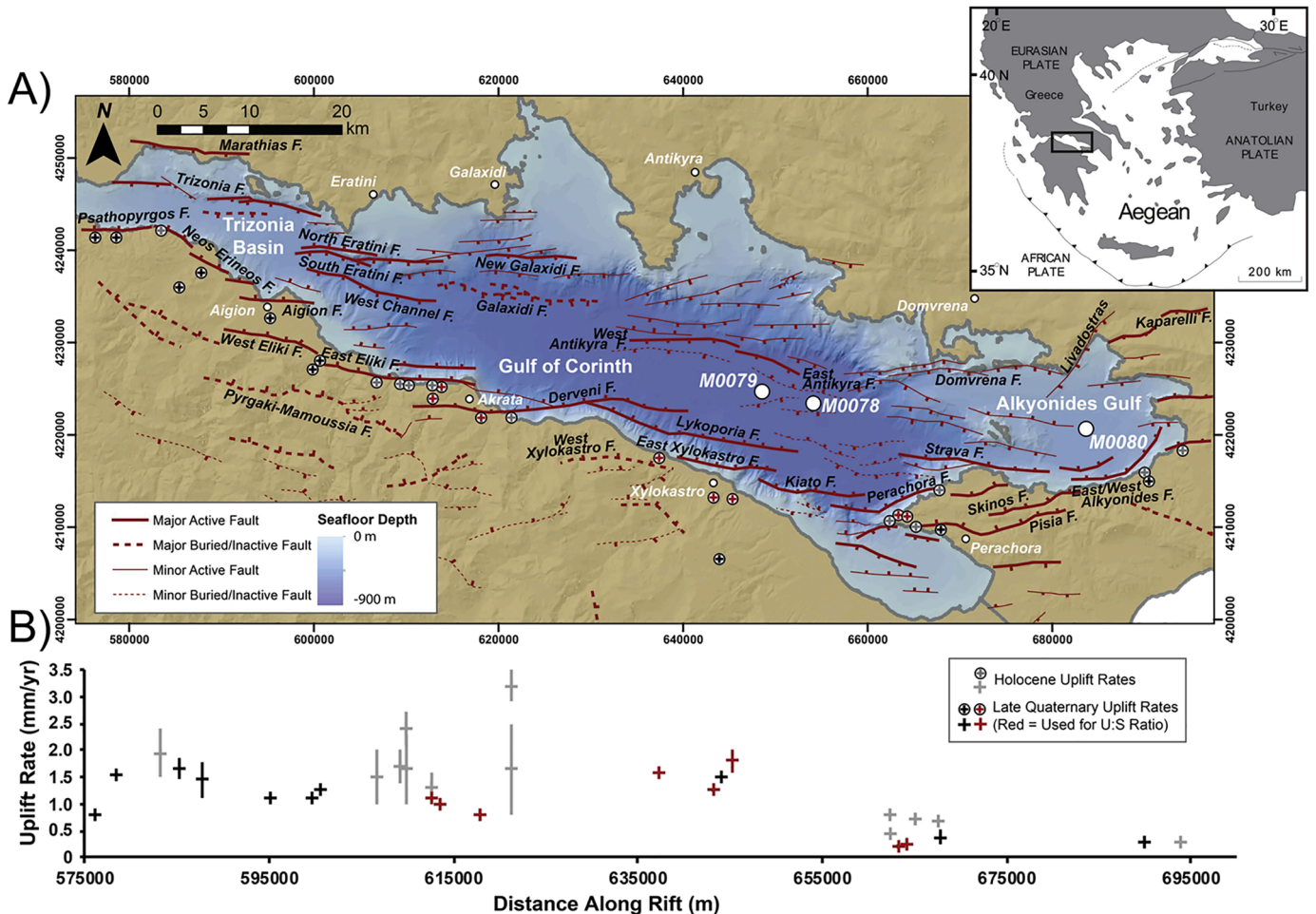Integration of onshore and offshore studies has helped identify 3

Fig 1. A) Structural map of the Corinth Rift, illustrating the onshore and offshore rift fault network and the location of three drillsites from IODP Expedition 381. Inset is a location map of the Corinth Rift within the tectonic framework of the Aegean. All major active faults offset the 129 kyr seismic horizon (see Figs. 2 & 3). Onshore faults are after Ford et al. (2017) in the west, Skourtsos and Kranis (2009) for the central rift, and Collier and Dart (1991) and Freyberg (1973) (1973) in the east. Offshore faults in the Gulf of Corinth and Alkyonides are after Nixon et al. (2016), and Beckers et al. (2015) in the Trizonia Basin. Bathymetry data courtesy of the Hellenic Centre for Marine Research collected for R/V Aegaeo cruises (Sakellariou et al., 2007). B) An along rift profile of late Quaternary and Holocene uplift rates (collated from Bell et al., 2009; Demoulin et al., 2015; Palyvos et al., 2010, 2007; Pechlivanidou et al., 2019; Roberts et al., 2009). The locations of the uplift data are shown on the structural map.

main rift phases since ~5 Ma (e.g., Armijo et al., 1996; Bell et al., 2009; Ford et al., 2017, 2013; Gawthorpe et al., 2018; Leeder et al., 2008; McNeill et al., 2019b; Nixon et al., 2016; Sachpazi et al., 2003; Taylor et al., 2011). A number of onshore faults south of the Gulf of Corinth (e. g., Fig. 1A) frame an early continental and lacustrine rift (Rift Phase 1). This was abandoned ~2 Ma, following a major northward shift in the locus of rifting to the location of the Gulf of Corinth, where deepening resulted from an increase in subsidence and sedimentation (Rift Phase 2). Since ~0.8 Ma (Rift Phase 3) the rift has evolved from a complex rift with varying geometry towards an asymmetric rift dominated by an active N-dipping border fault system, which has been responsible for considerable late-Quaternary uplift rates (>2 mm/yr; Bell et al., 2009; de Gelder et al., 2019) along the southern margin (Fig. 1B). These changes in rift polarity and progressive strain localisation within the rift have been well documented, however, due to a previous lack of absolute geochronology, the exact timescales of these processes and the details of how slip rates and activity on the rift fault network evolved are yet to be fully resolved.

Results from IODP (International Ocean Discovery Program) Expedition 381 provide, for the first time, an accurate and precise geochronology for the most recent ~2 Myrs of offshore syn-rift sediments (McNeill et al., 2019a, b). The combination of these temporal constraints with a detailed fault and stratigraphic framework from integrated offshore seismic reflection data (Nixon et al., 2016) provide an opportunity to investigate and quantify the early rift fault activity at higher spatial (i.e., 100–1000 m) and temporal scales (i.e., 100 kyr) than before. In this study we focus on the active rift fault network in the central Corinth Rift (i.e., Eratini to Perachora in the Gulf of Corinth; Fig. 1A) that initiated at the start of Rift Phase 2, documenting its development through the transition into Rift Phase 3 and to present day. The objectives are: 1) Illustrate spatio-temporal changes in fault activity

within the early rift fault network over the past ~2 Myr; 2) Characterise the distribution of strain within the rift fault network during changes in rift polarity and strain localisation; 3) Quantify the magnitude and distribution of fault slip rates along the active rift border fault system as it becomes established; and 4) Discuss the implications for earthquake potential within the developing rift system.

2. IODP Expedition 381: drill sites, age constraints and seismic stratigraphy

2.1. Drill sites

In October-December 2017, IODP Expedition 381 drilled and cored the last ~1–3 Myr of syn-rift sediments within the offshore Corinth Rift, to a maximum depth of 705 mbsf (McNeill et al., 2019a). This long and high-resolution record of early continental rifting provides key insights into changing basin environmental conditions and the first absolute age constraints of the offshore syn-rift stratigraphy, allowing rates and timings of rift tectonic and sedimentary processes to be determined. In addition, downhole logging and core physical properties provide detailed measurements of velocity, density and porosity for the offshore sediments, essential for accurately depth-converting seismic stratigraphy and decompacting the syn-rift sediments. The expedition drilled three sites (Fig. 1A): Site M0080 in the Alkyonides Gulf and Sites M0078 and M0079 in the central Gulf of Corinth. Here we focus on the age constraints in the central Gulf and their correlation to the seismic stratigraphy.

Site M0078 is located on a fault-bounded horst block and retrieved a long, condensed record of the syn-rift stratigraphy (Fig. 2A), whereas Site M0079, located within the primary depocentre, recovered an expanded high-resolution section of the most recent rift phase (Fig. 2B).
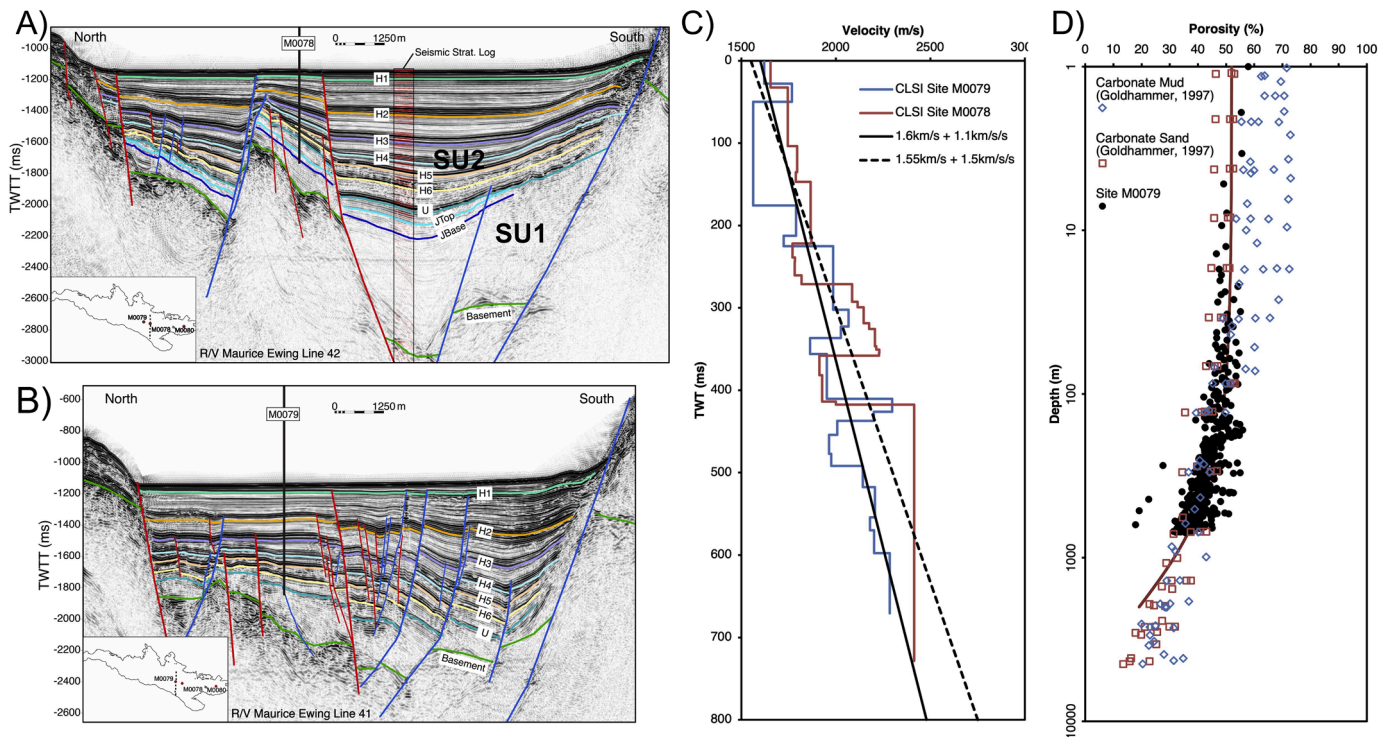

Fig 2. North to south seismic reflection profiles in Two-Way-Travel-Time (TWTT) crossing through the IODP 381 sites M0078 and M0079. (A) R/V Maurice Ewing Line 41, across Site M0079, and (B) R/V Maurice Ewing Line 42, across Site M0078. Key interpreted seismic horizons are after Nixon et al. (2016) and include: horizons H1-H6, representing the base of marine sub-units; the basin wide unconformity (U) between Seismic Units 1 and 2 (SU1 & SU2; Lithostratigraphic Units 2 and 1); the position of the top and base of the Jaromillo paleomagnetic sub-chron identified at Site M0078 (JTop & JBase), and the top of the pre-rift basement. North and south dipping faults are interpreted in blue and red, respectively. C) Velocity-time profiles derived from CLSI at IODP Sites M0078 and M0079. The dashed black line is the linear velocity model from Nixon et al. (2016) and the solid black line is the refined linear velocity model used in this study. D) A porosity-depth profile from IODP Site M0079, compared with experimental porosity data for carbonate muds and sands from Goldhammer (1997).

The cores reveal a sedimentary sequence dominated by fine-grained, distal turbiditic and hemipelagic deposits, which are divided into two lithostratigraphic units (Fig. 3) (Gawthorpe et al., 2022; McNeill et al., 2019b). The upper Lithostratigraphic Unit 1 (LU1) comprises subunits that alternate between predominantly homogeneous, bioturbated muds deposited in "marine" conditions and laminated/bedded muds deposited in "isolated" conditions when the basin was partially or fully cut-off from the open marine conditions of the Mediterranean. These subunits are distinguished by different abundances of marine and non-marine microfossil assemblages (Figs. 3B and C) (McNeill et al., 2019a, b). The cyclical changes in basin paleoenvironment are indicative of glacio-eustatic sea-level fluctuations, confirming previous interpretations that suggested isolated conditions in the basin correspond to when sea-level fell below the height of the basin sills (i.e., Rion Sill in the West, Corinth Isthmus in the East; McNeill et al., 2019b). Sediments in the lower Lithostratigraphic Unit 2 (LU2) are more homogeneous and lack the cyclicity observed in the overlying LU1, instead being dominated by intensely bioturbated non-marine muds that indicate a predominantly isolated basin (McNeill et al., 2019a). Therefore, the unit boundary (677 mbsf at Site M0079, 385 mbsf at Site M0078; Figs. 3B and 4C) marks the onset of repeated connections to the open ocean. McNeill et al. (2019a) contains detailed descriptions of the lithologies, microfossil assemblages and core physical properties of these units and subunits.

2.2. Age constraints

Core magnetostratigraphy, biostratigraphy and radiometric dating provide the first absolute age framework for the offshore Corinth Rift (Fig. 3A). The Brunhes-Matuyama paleomagnetic chron boundary (773 ka) near the base of LU1 provides an age of ~790 ka for the unit boundary (Maffione and Herrero-Bervera, 2022). Below the unit boundary at Site M0078 is a paleomagnetic interval of normal polarity (519–575 mbsf; Fig. 3C) representing the Jaramillo Subchron (1001–1076 ka), which is the only age constraint within LU2 (McNeill et al., 2019a). Biostratigraphic markers within LU1 (McNeill et al., 2019b) include: 1) Last Occurrence (LO) of *Pseudoemiliania lacunosa* (430 ka); 2) First Occurrence (FO) of *Emiliania huxleyi* (290 ka); and 3) crossover in dominance between *E. huxleyi* and *Gephyrocapsa* within sub-unit 1–2 (~70 ka in the Mediterranean; Anthonissen and Ogg, 2012). The latter (3) is expected at the base of subunit 1–2, supported by a radiocarbon date (34.5 +/- 0.7 ka) midway through the subunit (Fig. 3A). Combining these age constraints allows correlation of the alternating marine and isolated subunits within LU1 to oxygen isotope stages and glacio-eustatic sea level (Fig. 3A). Precise ages obtained for the subunit boundaries are based on a sill depth of ~60 m (present-day depth of the Rion Sill) and the eustatic sea-level curve of Spratt and Lisecki (2016), which works well down to the base of subunit 1–13 at ~535 ka (Fig. 3; McNeill et al., 2019b). There is evidence for more marine incursions between the LU1-LU2 unit boundary and subunit 13, however, absolute dates are needed to correlate these to oxygen isotope stages. These subunit boundaries can be correlated between Sites M0078 and M0079 (Fig. 3).

2.3. Seismic stratigraphy

Deep penetrating multi-channel seismic reflection data collected in the Gulf of Corinth by the R/V *Maurice Ewing* in 2001 (e.g., Figs. 1 and 2) image a complete syn-rift sedimentary succession, up to ~2.7 km thick, recording basin evolution and depocentre development over the past ~2 Myrs (i.e., Rift Phases 2 and 3) (Bell et al., 2009; Nixon et al., 2016; Taylor et al., 2011). Key seismic horizons (Figs. 2 and 3D) and faults were previously interpreted in detail by Nixon et al. (2016), forming the basis for locating the IODP drillsites and the analysis in this study. The succession is divided into two seismic stratigraphic units, equivalent to the two lithostratigraphic units, separated by a locally angular

unconformity (horizon U), which represents the transition from Rift Phase 2 to 3 (Fig. 2A). The older Seismic Unit 1 (SU1) corresponds with LU2 and is characterised by low-amplitude and less coherent seismic reflectors, whereas the younger Seismic Unit 2 (SU2) corresponds with LU1 and is well-stratified with alternating packages of high- and low-amplitude reflectors (Fig. 2A). On the basis of shallow piston cores (e.g., Moretti et al., 2004) and marginal clinoform sequences (e.g., Bell et al., 2009), the alternating high- and low-amplitude packages in SU2 were originally interpreted to record ~100-kyr glacio-eustatic cycles representing highstand and lowstand conditions, respectively (e.g., Bell et al., 2009; Nixon et al., 2016; Sachpazi et al., 2003; Sakellariou et al., 2007; Taylor et al., 2011). An integrated seismic stratigraphic model by Nixon et al. (2016) hypothesised six glacio-eustatic cycles within SU2, with seismic horizons H1-H6 (Fig. 2) marking the base of high-amplitude packages and the onset of marine highstand conditions.

Core-Log-Seismic Integration (CLSI) during IODP Expedition 381 tied data from Sites M0078 and M0079 to the seismic reflection data collected by the *R/V Maurice Ewing*. Synthetic seismograms, calculated from density and velocity information from downhole logging and core physical properties, indicate that intervals of high reflectivity correspond with marine subunits in LU1 (McNeill et al., 2019a), thus confirming the seismic character of highstands/lowstands interpreted by previous authors. Matching prominent reflections in the synthetic with reflections in the data (i.e., Fig. 2) allows stratigraphic correlation between the boreholes (Fig. 3A-C) and the seismic data (Fig. 3D). At Site M0078, the Jaramillo Subchron within LU2 can also be tied to seismic reflectors (i.e., horizons JTop and JBase; Figs. 2A and 3D) and locally traced along seismic profiles around the drill site, providing age constraints within SU1. By applying the age constraints for the unit boundary (U = ~790 ka) and within SU1 (JBase = ~1076 ka) to an expanded section of the sedimentary succession (south of Site M0078; Fig. 2A), representing a close-to-complete basin sedimentary record, and extrapolating decompacted sedimentation rates from SU2 and the upper part of SU1 gives an age estimate of ~2.5–2 Ma for the oldest offshore sediments (Fig. 3D). These new and absolute horizon ages provide the framework for determining rates of fault activity and timeframes for basin and depocentre development.

3. Determination of fault slip rates

Several studies have attempted to quantify slip rates for major faults throughout the Corinth Rift using a variety of techniques including: palaeoseismological trenching (e.g., McNeill et al., 2005a; Palyvos et al., 2005); cosmogenic dating of fault planes (e.g., Mechernich et al., 2018); fault drilling (e.g., Cornet et al., 2004); seismic data (e.g., Beckers et al., 2015; Bell et al., 2009); and derivation from uplifted marine terraces and fauna by combining with dislocation modelling/seismic data or applying an Uplift : Subsidence (U:S) ratio (e.g., Armijo et al., 1996; de Gelder et al., 2019; McNeill and Collier, 2004). A compilation of late Quaternary estimates in Bell et al. (2009) shows highest slip rates (~3–5 mm/yr) for the Eliki, Derveni, Lykoporia and Xylokastro faults along the southern margin of the central rift, and some studies even suggest rates of up to 9 mm/yr for these faults (e.g., de Gelder et al., 2019). In contrast, late Quaternary fault slip rates along the northern margin are much lower (<2 mm/yr; Beckers et al., 2015; Bell et al., 2009). However, these slip rate estimates are averaged over different time periods defined either by the uplift/subsidence age or by the age of the fault, the latter commonly being imprecise. Furthermore, some estimates combine subsidence and uplift rates of different ages to calculate an average slip rate (e.g., de Gelder et al., 2019). This makes it unreasonable to spatially compare the data as they are likely influenced by temporal slip rate variations on faults. Ultimately there is a need for a consistent quantification and comparison of fault activity through time to decipher spatial and temporal variations, and to have a better representation of current fault activity throughout the rift.

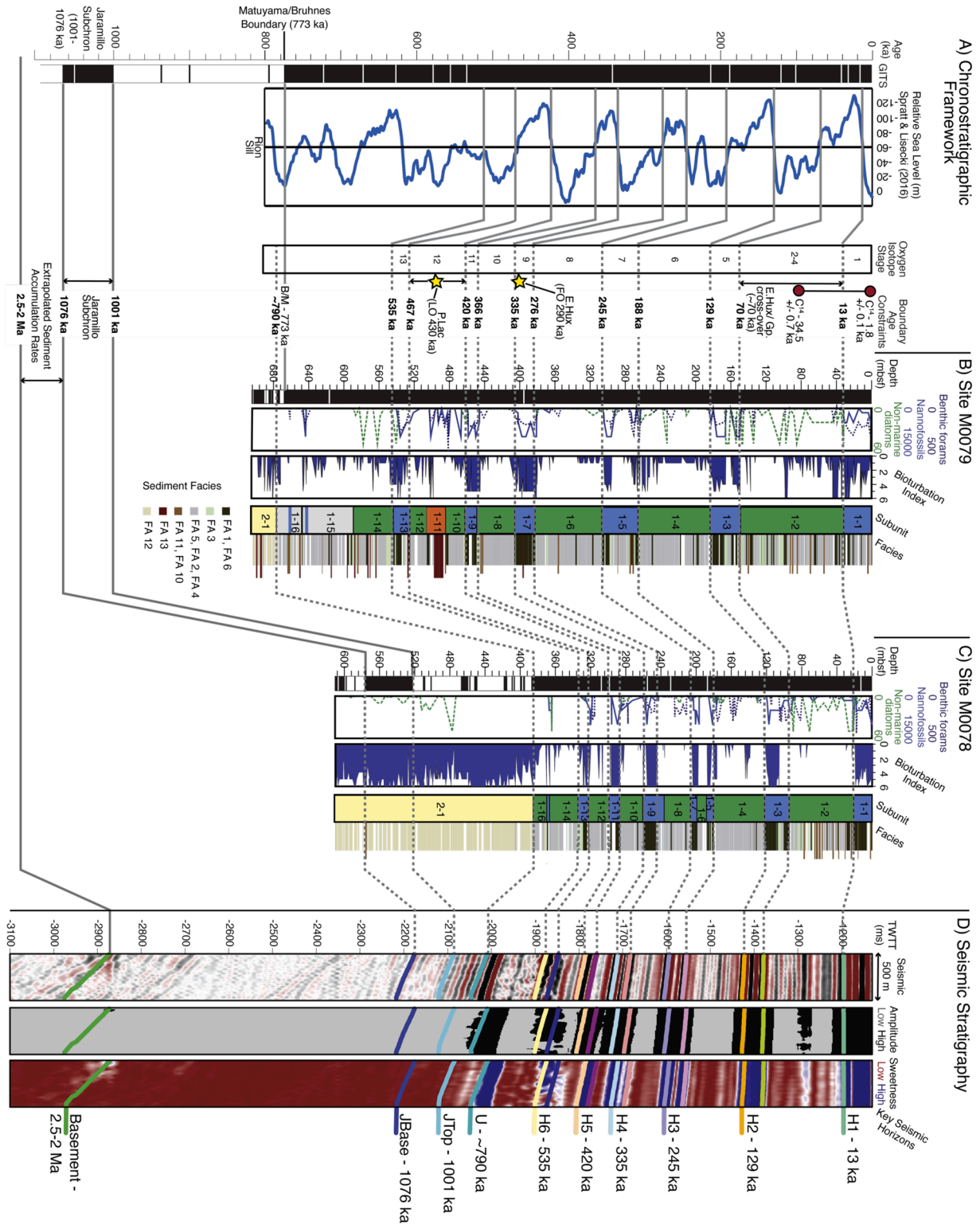By integrating the IODP Expedition 381 results with the existing

Fig 3. A-C) Stratigraphic correlation between sites M0079 and M0078 with eustatic sea-level (after Spratt & Lisecki, 2016) and Marine Isotope Stages (MIS) showing main stratigraphic subunits (blue for marine, green for isolated/semi-isolated environments, grey for undetermined environment, orange sub-units are slumped intervals, and yellow denotes Lithostratigraphic Unit 2) and selected bed types within Lithostratigraphic Units 1 and 2. The location of minimum and maximum radiocarbon ages (C^{14}) are shown as red circles and key biostratigraphic markers are shown with yellow stars. Abundance/counts of calcareous nannofossils (light blue), benthic foraminifera (dark blue, dotted) and non-marine diatoms (green, dashed), bioturbation index, paleomagnetic results and IODP 381 lithostratigraphic subunits for each site are from McNeill et al. (2019a). D) Shows the correlation of subunit boundaries and their associated ages with seismic stratigraphy and key horizons.
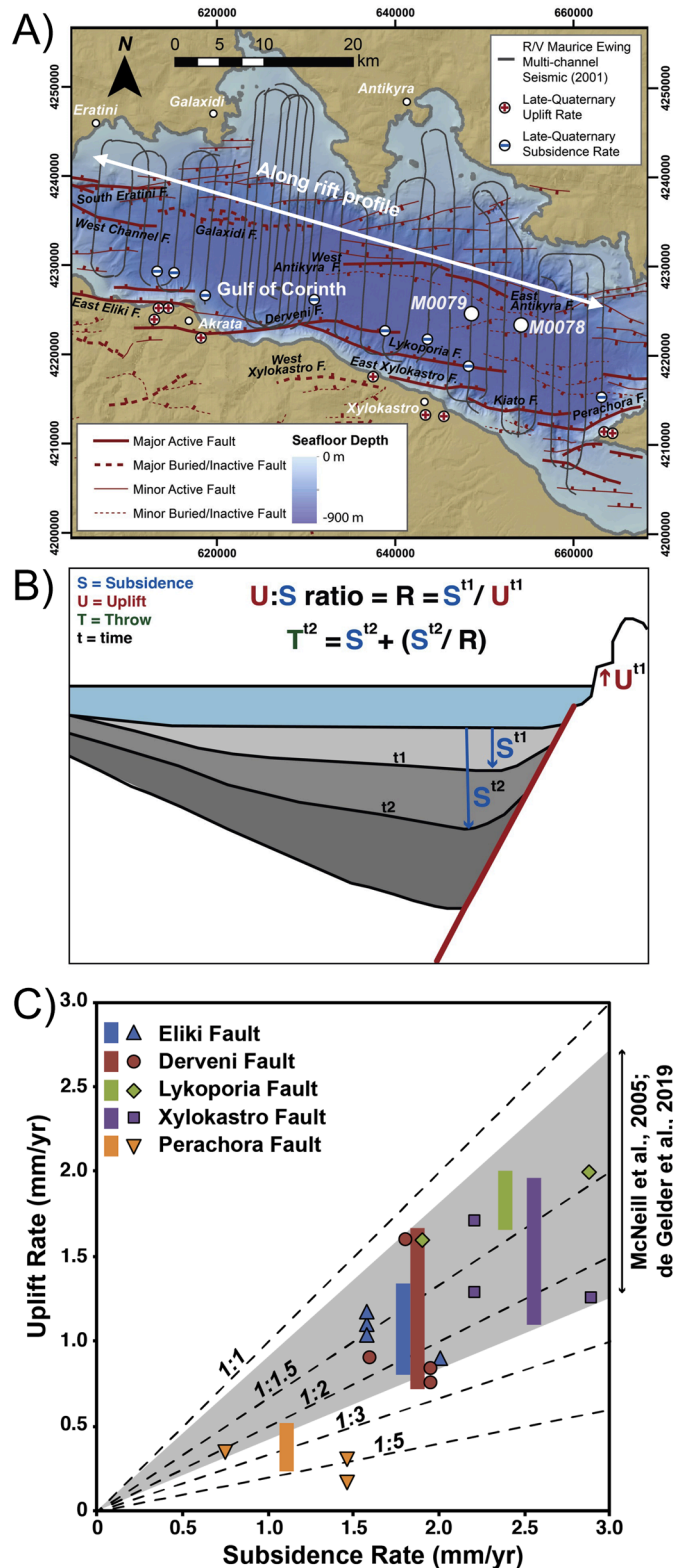
Fig 4. A) Zoomed map of the Gulf of Corinth (central Corinth Rift) showing the position of IODP Sites M0078, M0079 and the N-S multichannel seismic reflection profiles collected by the R/V Maurice Ewing. The location of uplift and subsidence estimates used to calculate uplift:subsidence ratios plotted in C) also shown. B) Schematic figure illustrating how fault throws were either directly measured (green) or extrapolated using uplift and subsidence data. C) Plot of uplift against subsidence for each major fault along the southern margin. Contours represent corresponding uplift:subsidence ratios, with solid colour bars showing the range of ratios for each fault.

seismic reflection data and plethora of onshore uplift data we can now significantly improve the fault slip rate estimates for the Corinth Rift. Moreover, the new absolute age constraints of the laterally continuous seismic horizons allow, for the first time, an investigation into how rates of fault activity change both spatially and temporally throughout the rift. Throw and subsidence, for both basement-cutting faults and those confined within the syn-rift sediments, were directly measured along the H2, H4, U and Basement horizons for 33 N-S seismic profiles along the Gulf of Corinth (Fig. 4A). The measured throw and subsidence values were converted from time to depth using a linear velocity model refined from the CLSI information at Sites M0078 and M0079, that increases from 1.6 km s^{-1} at the seafloor by 1.1 km s^{-1} s^{-1} (Fig. 2C). Values were decompacted using a porosity-depth relationship constrained from porosity measurements at Site M0079 (Fig. 2D; McNeill et al. 2019a). The resulting throw and subsidence values are used to calculate throw and subsidence rates along each fault for the time periods between the key horizons (H2, H4, U, Basement).

For the majority of faults, throw was calculated from the hanging wall and footwall cut-offs of each horizon (Fig. 4B). However, for the major N-dipping faults that straddle the southern margin coastline, only the hanging wall stratigraphy is imaged allowing just one component of throw to be measured (i.e., hanging wall subsidence). Throw estimates for these faults were calculated by applying individual uplift:subsidence ratios (U:S) for each major fault (i.e., Fig. 4C) to estimate the footwall uplift component of the throw (Fig. 4B). The fault specific U:S ratios combine previously published late Quaternary uplift rates with subsidence rates from this study that are a) averaged over the same time period and b) located in the immediate footwall and hanging wall of the given fault. Ratios for the Eliki, Derveni, Lykoporia and Xylokastro Faults fall within the range of 1 : 1.1–2.6, whereas the Perachora Fault ranges from 1 : 2.1–4.7, possibly affected by subsidence of its immediate footwall associated with recent activity on the Pisia Fault onshore. Overall, the U:S ratios closely match those predicted by visco-elastic models (i.e., 1:2.2–3.1, Bell et al., 2018) and previous late Quaternary estimates used in the Corinth Rift (e.g., 1 : 1.2–2.2, McNeill et al., 2005a; 1 : 1.1–2.4, de Gelder et al., 2019). As the current basin is underfilled with a substantial water column (Fig. 1A), and the paleobathymetry is unknown, the measured subsidence and resulting throws are minima. However, this underestimate is thought to be minimal after sediment decompaction, which accounts for much of the basin underfill. Slip rates were calculated using an average dip of 50° for faults in the Trizonia Basin and Gulf of Corinth, based on observations from seismic data (e.g., Bell et al., 2009; Nixon et al., 2016) and exposed fault scarps (e.g., Ford et al., 2013). However, an observed shallower fault dip of 45° is used for the Perachora Fault, matching fault dips to the east and in the Alkyonides Gulf (e.g., Leeder et al., 2005). The range in uplift rates (Fig. 1B) and subsequent U:S ratios for each fault (Fig. 4C) provide error margins for the throw and slip rate estimates presented for the southern margin faults.

4. Distribution of activity throughout the rift fault network

The fault network in the central Corinth Rift (Fig. 5) is dominated by a right-stepping array of major N-dipping faults bounding its southern margin (Eliki, Derveni, Lykoporia, Xylokastro, Kiato and Perachora faults) and major S-dipping faults bounding its northern margin (South Eratini, West Channel, Galaxidi and Antikyra faults) that have basement throw offsets >700 m. These bound a ~3-km-thick depocentre that lies along the WNW-ESE trending rift-axis. Numerous smaller faults also cut the basement, forming small horsts within the rift axis (e.g., north of Xylokastro) and deforming the shelf along the northern margin (e.g., Galaxidi Bay and Antikyra Bay). An along-rift profile of cumulative basement throw for the offshore rift fault network mimics the top basement depth map with two peaks that align with the two deepest top basement locations and decreasing to the east and the west where basement shallows and the rift narrows (Fig. 5C and D). The amount of
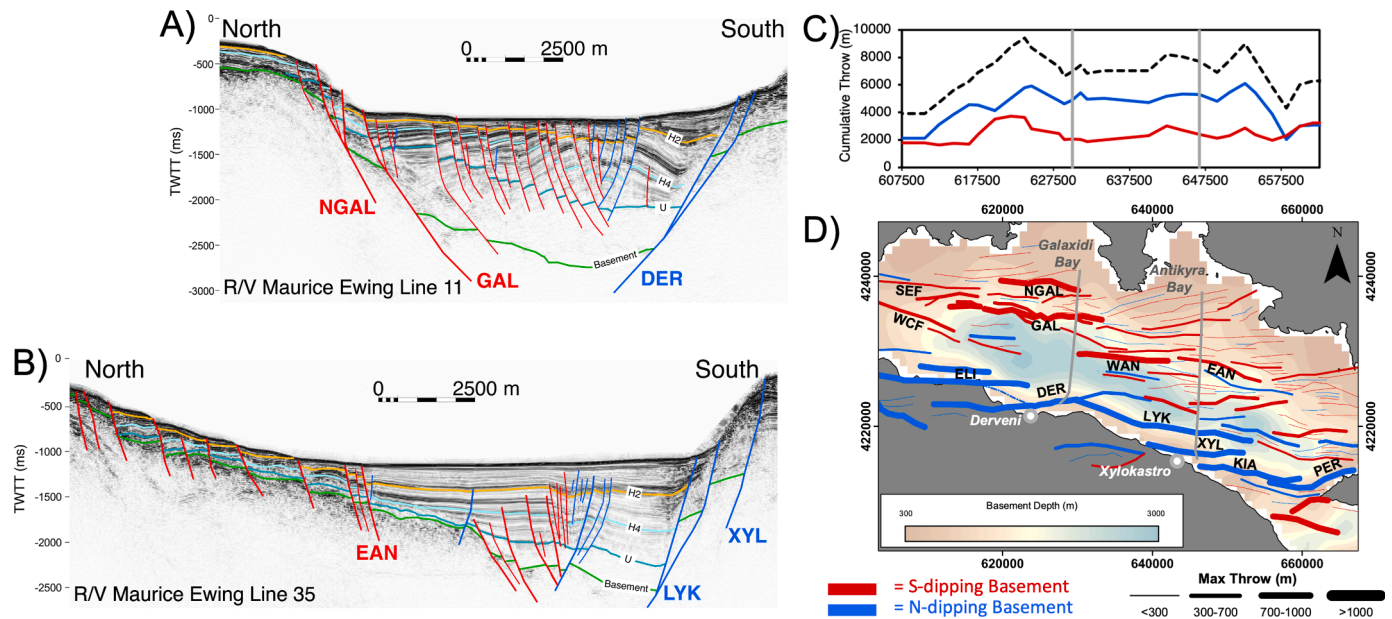
Fig 5. A) and B) are north to south seismic reflection profiles in Two-Way-Travel-Time (TWTT), illustrating rift geometry and fault activity/timing. In A) a polarity change can be seen with sediment thickening in the hanging wall of the Galaxidi Fault below horizon U, followed by thickening into the Derveni Fault above horizon H4. North of the East Antikyra Fault and the Galaxidi Fault, numerous south-dipping faults can be seen offsetting horizon H2 with some producing scarps at the seafloor. C) Along rift profile of cumulative throw for all basement cutting faults. Blue and red lines represent N- and S-dipping faults, respectively, and the dashed line is the combined profile. D) Structural map of basement depth basement cutting faults for the Gulf of Corinth. The location of the seismic reflection profiles are shown in grey on both C) and D). Fault names: SEF = South Eratini Fault, WCF = West Channel Fault, ELI = Elike Fault, NGAL = New Galaxidi Fault, GAL = Galxidi Fault, DER = Derveni Fault, WAN = West Antikyra Fault, EAN = East Antikyra Fault, LYK = Lykoporia Fault, XYL = Xylokastro Fault, KIA = Kiato Fault, PER = Perachora Fault.

deformation accommodated by S-dipping faults is relatively constant along the rift, contributing approximately one third of the total throw (Fig. 5C). In contrast, the N-dipping faults form more of a bell-shaped throw profile and contribute approximately two thirds of the total throw. The bell-shaped profile is partially exaggerated due to the omission of onshore faults to the west (e.g., Pirgaki-Mamoussia Fault) and the east (e.g., Pisia Fault) where the offshore rift narrows.

A break-down of the cumulative fault throw rates into four time intervals between ~2 Ma and the present day indicates how the distribution of deformation throughout the rift network has changed temporally (Figs. 6 and 7). Between ~2 Ma and ~130 ka the fault network accommodated an average cumulative throw rate of ~3–4 mm/yr (Fig. 6A-C). Over this time period the proportion of deformation accommodated by S-dipping faults decreased from ~40 % to ~15 %. This corresponds to decreasing throw rates on the major S-dipping Galaxidi, West Antikyra and East Antikyra faults, along with the development of numerous distributed minor S-dipping faults along the northern margin shelf (Fig. 7A–C). The Galaxidi fault shows the greatest decrease in activity, evolving from a significant depocentre-controlling fault prior to ~790 ka (Fig. 7A) to a segmented array of minor S-dipping faults by ~130 ka (Fig. 7C).

In contrast, activity increased on the major N-dipping faults that bound the southern margin during this time period (Fig. 7A–C), with a significant increase in activity between ~335–130 ka. N-dipping faults accommodated ~85 % of the total deformation during this time interval (Fig. 6C). This significant increase in activity on major N-dipping faults results in an asymmetric rift and a southerly shift in depocentre locations – from the hanging walls of major S-dipping faults (e.g., Galaxidi Fault; Fig. 7A) to the hanging walls of major N-dipping faults (e.g., Derveni and Lykoporia Faults; Fig. 7C). Coincident with this rift polarity change is the development of numerous minor faults along the rift axis that are confined to the syn-rift sedimentary sequence, accommodating tilting and flexure as activity shifted between the northern and southern margin-bounding faults (Fig. 7B and C).

Since ~130 ka, average cumulative throw rates for the fault network have increased by a factor of 2 to >6 mm/yr, peaking at 10 mm/yr and 8 mm/yr offshore Xylokastro and Derveni, respectively (Fig. 6D). Increased activity on major N-dipping faults is maintained during this time interval, creating a single large depocentre offshore Xylokastro (Fig. 7D). However, the increased activity on the N-dipping faults only explains part of the overall increase in cumulative throw rate. Instead, this is also attributed to increased activity on the numerous S-dipping faults deforming the northern shelf, as seen in Antikyra Bay and Galaxidi Bay. Furthermore, new major S-dipping faults (e.g. South Eratini and New Galaxidi Faults; Fig. 7D) have established themselves, collapsing the footwall of the previous S-dipping margin-bounding faults. This increased faulting on the northern margin indicates a widening of the active deformation zone within the rift and coincides with the establishment of an asymmetric half-graben controlled by increased activity on the prominent N-dipping border fault system.

5. Increasing slip rates and kinematic linkage of the border fault system

As is evident from the throw rate maps (Fig. 7), the major N-dipping faults of the southern margin border fault system play an important role in the evolution of the rift, accommodating the majority of recent deformation and controlling rift asymmetry. Averaged slip rates for these major southern margin faults have been estimated by various authors (e.g., Bell et al., 2009; de Gelder et al., 2019; McNeill and Collier, 2004), but these tend to consider the last few 100 kyr and only in a few locations, making it difficult to assess the evolution of the border fault system. The precise age and numerous measured throw data in this study allow detailed along-strike profiles of slip rate for each fault (Fig. 8), illustrating how fault activity varies spatially as the border fault system became established over the past ~2 Myr.

Between ~2 Ma and 790 ka, slip rate distributions along each individual fault form approximately symmetrical, convex-up profiles
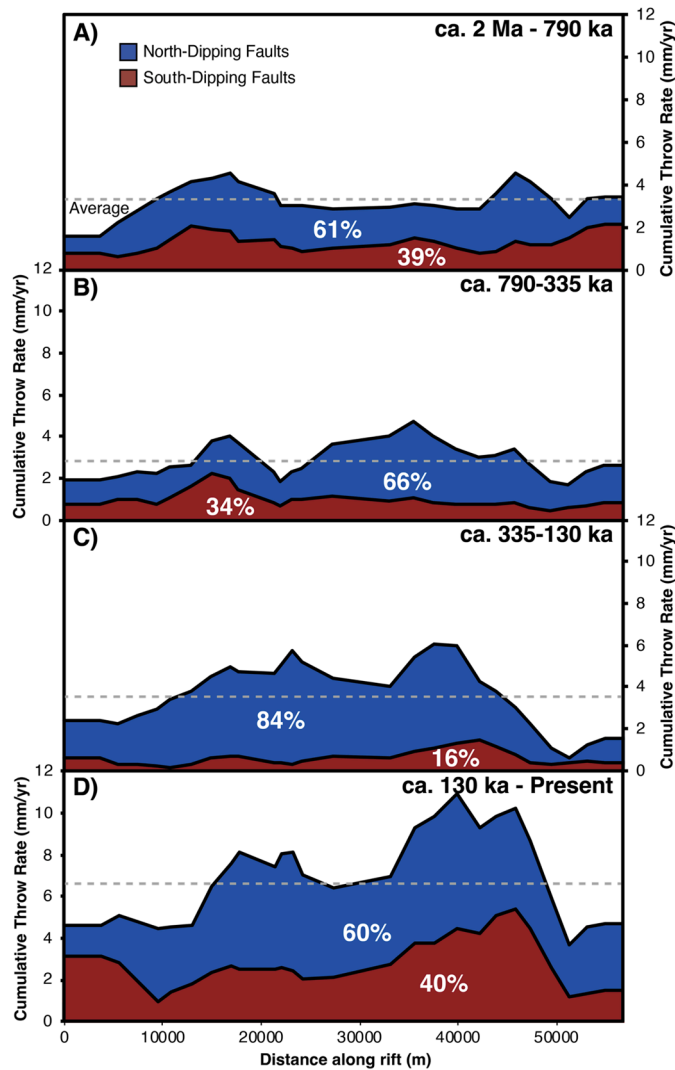
Fig 6. Stacked profiles of cumulative throw-rate along the rift for different time intervals over the last 2 Myr: A) 2 Ma – 790 ka; B) 790–335 ka; C) 335–130 ka; D) 130 ka – Present Day. The stacks and corresponding percentages compare the contribution of all the N-dipping faults (blue) and S-dipping faults (red) that offset basement. Note how overall throw-rates increase with time and how the proportion of deformation accommodated by N-dipping faults increases from A-C.

(Fig. 8A). The Eliki, Derveni, Lykoporia and Kiato faults exhibit peak slip rates of 2 to 2.6 mm/yr, whereas the Xylokastro and Perachora faults were less active with peak slip rates of <1 mm/yr. The cumulative profile identifies three broad slip rate highs at approximate distances of 20,000 m, 40,000 m and 50,000 m along-strike. These highs correspond with three kinematically separate fault segments of the border fault system at this time. To the west, the Eliki and Derveni faults are clearly kinematically linked, forming a bell-curved slip rate profile that represents a ~40-km-long fault segment (segment i; Fig. 8A). The combined slip rates of the Lykoporia and Xylokastro faults form a bell-curved profile of another kinematically-coherent fault segment, ~20-km-long, in the centre of the border fault system (segment ii; Fig. 8A). To the east, the Kiato and Perachora faults form a third kinematically-coherent fault segment, ~20-km-long, with a bell-shaped profile (segment iii; Fig. 8A).

A small increase fault slip rates occurs between ~790 and 335 ka, with peaks >2 mm/yr along all faults and a slip rate high of 4.7 mm/yr on the Lykoporia fault. The slip rate profiles of the Lykoporia and Xylokastro faults are asymmetric with steep gradients towards their eastern tips, whereas the Kiato and Perachora faults have asymmetric

profiles with steep gradients towards their western tips. This reflects kinematic interaction between fault segments ii and iii (Fig. 8A), which now form a kinematically-coherent slip rate profile (segment ii-iii; Fig. 8B). This segment ii-iii slip rate profile is ~40-km-long and asymmetric, with a slip rate high and steep gradient close to its western tip, indicating kinematic interaction with fault segment i to the west.

Activity significantly increases on all faults between ~335 and 130 ka, with the exception of the Perachora fault. In particular, maximum slip rates observed on the Derveni and Lykoporia faults double to >7 mm/yr during this time interval. As a result, fault segments i and ii-iii have very asymmetric slip rate profiles with peaks and steep profile gradients towards their eastern and western tips, respectively. This indicates clear kinematic interaction between the two segments, which are linked in plan-view at ~30,000 m distance along-strike. Despite being linked and kinematically interacting there is still a slip rate low between the two segments, thus the border fault system is not kinematically coherent and linkage of segments i and ii-iii is not fully established at this time.

Over the last ~130 kyr the border fault system has become kinematically coherent, with a broad, bell-shaped cumulative profile. Slip rates along segment i-ii-iii are generally >5 mm/yr with a maximum of 7.7 mm/yr on the Lykoporia fault, maintaining the increased slip rates of the previous time interval. Only the Eliki-Derveni-Lykoporia faults are connected in plan-view (Fig. 7D), however, the kinematic coherence of the border fault system indicates that all faults are likely to be connected at depth forming a high slip rate, >65 km long, crustal-scale border fault.

6. Discussion

6.1. A story of strain localisation, fault linkage and margin deformation

The well constrained timing and high temporal resolution of this study has allowed us to document changes in the distribution of fault activity throughout an active rift fault network in greater detail than before. We identify three stages in the development of the central Corinth Rift fault network over the past ~2 Myr (Fig. 9): 1) strain transfer and localisation; 2) fault linkage and acceleration of fault slip rates; and 3) establishment of a kinematically-coherent border fault system, with flexure and deformation of the subsiding rift margin. These stages are all linked to the increasing slip rates and development of a crustal scale rift border fault system.

An initial stage of strain localisation involves the steady transfer of strain from major S-dipping faults onto major N-dipping faults from ~2 Ma to 335 ka (Fig. 9A). During this process, activity on major S-dipping faults decreases, instead of abruptly ceasing, while activity on the major N-dipping faults of the segmented border fault system increases (i.e., Figs. 6A–C and 7A–C). Progressive strain localisation is commonly observed as an important process in the development of rift and passive margin fault networks (e.g., Cowie et al., 2005; Gawthorpe et al., 2003; McLeod et al., 2000; Walsh et al., 2003). A common theme in these studies is the death of the surrounding fault network as strain localises onto a main fault. Here we do not observe this, instead there is a systematic decrease in activity rates and a gradual transfer of strain onto the border fault system. This stage of decreasing activity is likely not observed in many rifts because of their coarse temporal resolutions (>10^6 yr), thus missing details of strain localisation.

At ~335 ka overall deformation increases, accommodated by the southern border fault system with an acceleration of fault slip rates, rapidly localising strain (Figs. 8C and 9B). Increasing slip rates during strain localisation are often attributed to activity ceasing on surrounding faults (e.g., Cowie et al., 2007) or to increases in extension rate (e.g., Nicol et al., 1997). Although the activity on major S-dipping faults continues to decrease ~335–130 ka, it cannot account for the accelerated slip rates on the southern border fault system. Instead, the marked increase in average slip rate is interpreted to correlate with linkage of
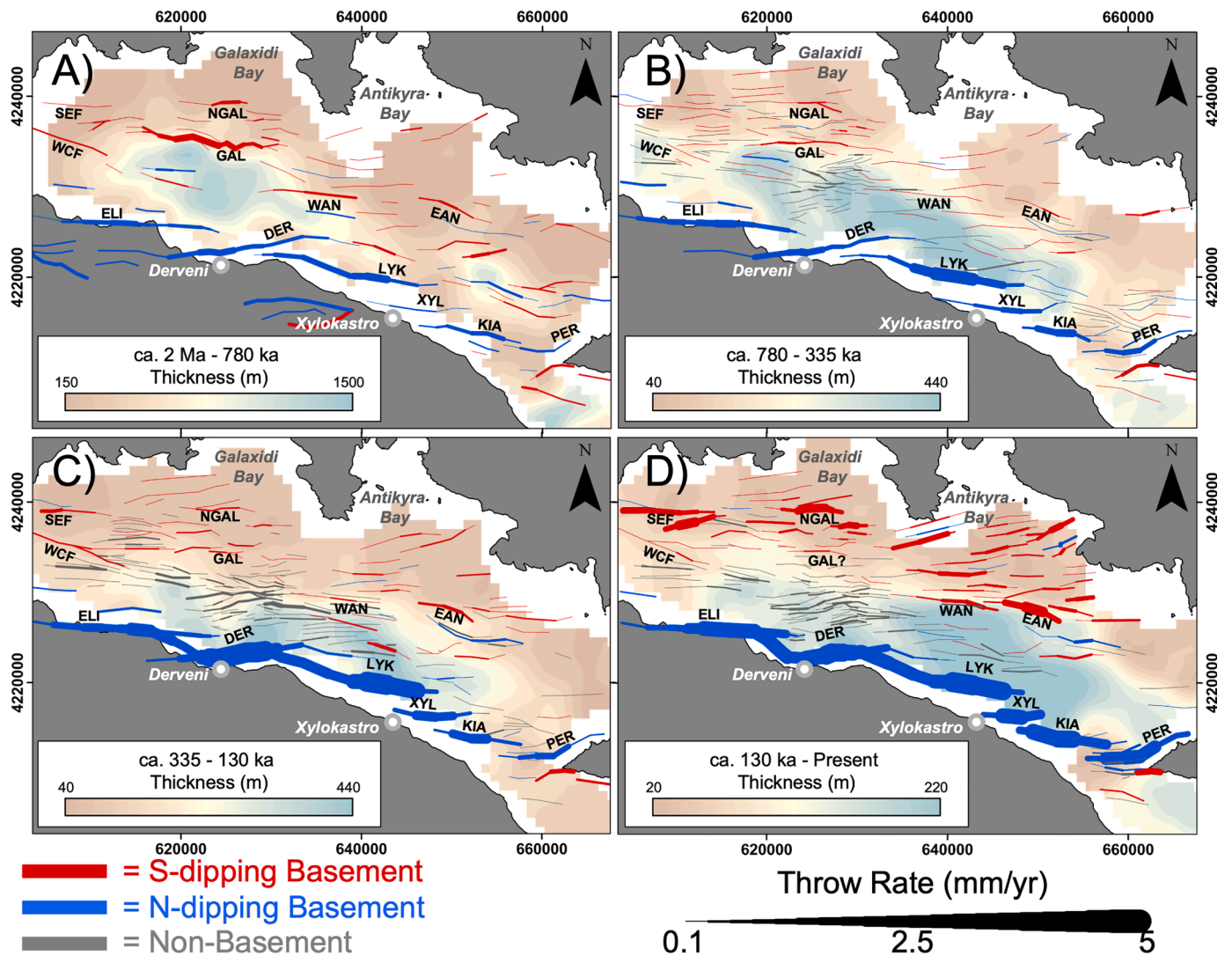
Fig 7. Fault maps showing the throw rates of each fault within the rift fault network and isopach maps for different time intervals over the last 2 Myr: a) 2 Ma – 790 ka; b) 790–335 ka; c) 335–130 ka; d) 130 ka – Present Day. See Fig. 5 for fault nomenclature.

the border fault system (segments i and ii-iii; Fig. 8C) and an increase in net cumulative fault slip rate across the rift (i.e., an increase in extension rate). Similar marked increases in fault slip rate following linkage have been observed for the Rangitaiki Fault in the Whakatane Graben over similar timeframes (10^5 yr; Taylor et al., 2004) and are also recognised in numerical models (Cowie et al., 2000). Our observations indicate that increasing slip rates on the border fault system are the combined result of strain transfer from the surrounding network, producing a gradual increase in fault slip rate, and fault linkage, resulting in a marked acceleration of slip rates. These two processes drive the rapid localisation of strain within the rift fault network, but also drive increased extension across the rift system.

After ~130 ka, there is a continued increase in slip rate on the border fault system as it becomes kinematically coherent (Fig. 8D). However, instead of seeing further localisation of strain onto this structure we observe an increase in both slip rates and the number of faults on the northern margin, widening the active deformation zone (Figs. 7D, 9C). At this stage of the rift's evolution, a subsiding flexural northern margin has developed in the hanging wall of the now established border fault system (e.g., Beckers et al., 2015; Bell et al., 2009; Pechlivanidou et al., 2019; Stefatos et al., 2002). With significant increases in slip rate on the border fault system after ~335 ka, increased deformation of the northern margin is likely a response to increased flexural downwarping of the

hanging wall (Fig. 9C; e.g., Lavier and Buck, 2002; Richter et al., 2021; Shillington et al., 2020). Hanging wall flexural deformation is often associated with listric fault geometries or fault bends at depth, however, the long-term geometry and morphology of the Corinth Rift supports a more planar fault geometry (i.e., Bell et al., 2018; Fernández-Blanco et al., 2020). Considering the border fault system was still establishing itself, it is expected that the fault plane would extend farther down-dip into the brittle crust as fault segments link and accrue more slip. Once a > 65-km-long, kinematically linked border fault system develops, with >3 km of basement offset, the fault plane would be a crustal-scale fault extending to the base of the brittle crust (e.g., Fernandez-Blanco et al., 2020) where changes in rheology may have resulted in the fault decoupling at the brittle-ductile transition zone. This interpretation helps explain the recent activity and broadening of the deformation zone on the northern margin and would agree with microseismicity patterns at the western end of the border fault system, offshore Aigion, at 9–12 km depth (e.g., Lambotte et al., 2014).

6.2. Long-term geological rates versus recent fault activity

High geodetic extension rates and intense seismicity are testament to the level of fault activity throughout the Corinth Rift, with frequent *Mw* >6 earthquakes in recent times (e.g., Bernard et al., 1997; Jackson et al.,
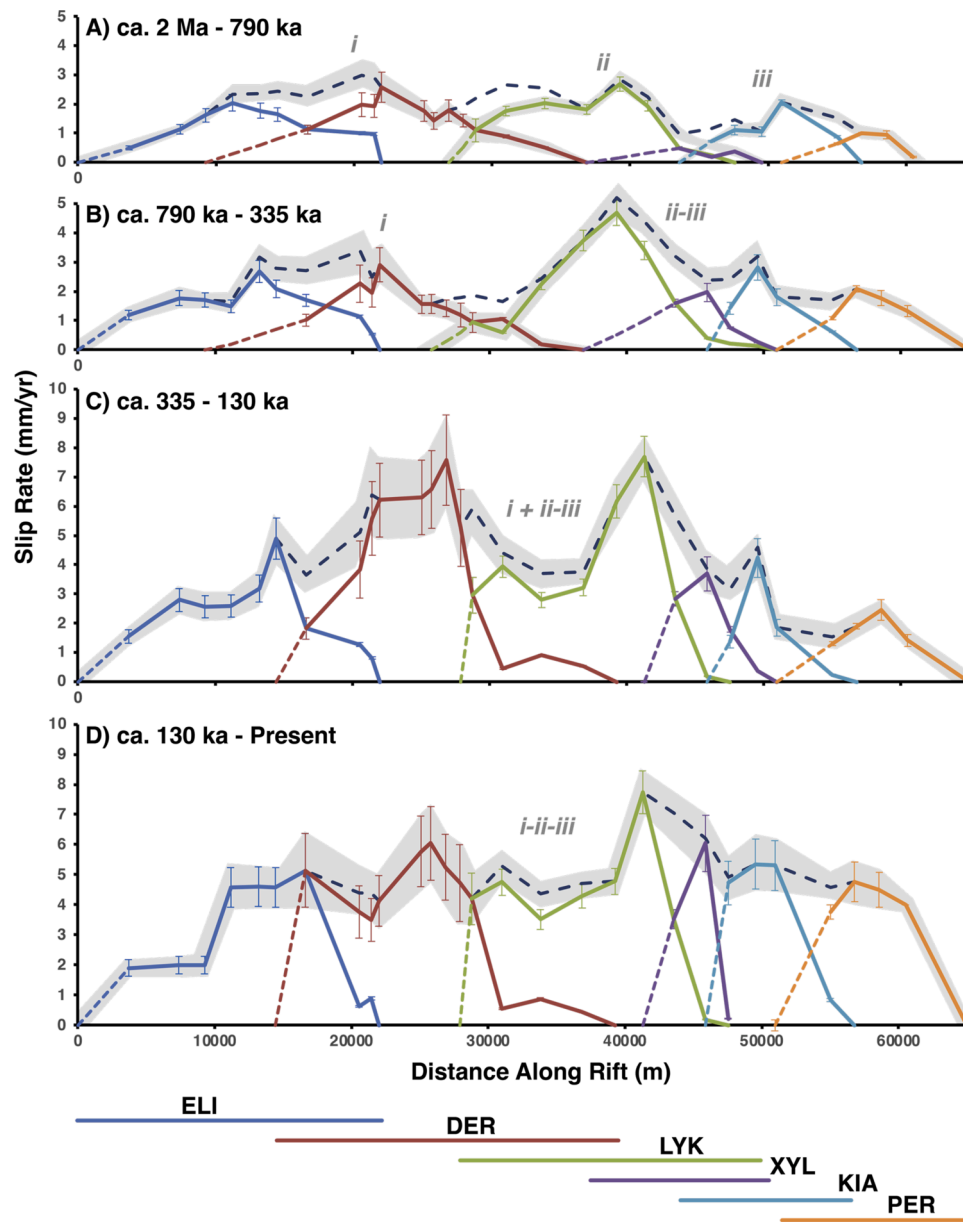
Fig 8. Slip-rate profiles for major N-dipping border faults from the southern margin of the Gulf of Corinth, illustrating their growth and linkage over the last 2 Myr: a) 2 Ma – 790 ka; b) 790–335 ka; c) 335–130 ka; d) 130 ka – Present Day. The dashed blacked line depicts the cumulative profile. Kinematically coherent segments of the border fault system (segments i, ii, iii, ii-iii and i-ii-iii) are shaded in grey. Error bars are based on the range of uplift:subsidence ratios used to estimate slip for each fault. A dip angle of 50° was applied for all faults apart from the Perachora Fault, which used a dip angle of 45°.

1982), microseismicity swarms (e.g., Lambotte et al., 2014) and a historical catalogue of destructive earthquakes (e.g., Papazachos and Papazachou, 2003). Geodetic extension rates vary spatially along the rift from <5 mm/yr in the Alkyonides Gulf to 11 mm/yr at Xylokastro in the central rift and up to 15–20 mm/yr in the western rift (Fig. 10A; Bernard et al., 2006; Briole et al., 2000; Clarke et al., 1998). However, it is important to understand these recent/geologically instantaneous records of deformation in the context of long-term rates and patterns of fault activity (e.g., Bell et al., 2011; Ford et al., 2017).

In Fig. 10, the late Quaternary slip rate data for the major southern margin border faults are extended to include faults in the Trizonia Basin and Alkyonides Gulf in the western and eastern parts of the rift, respectively. Only the footwall uplift component of displacement is constrained for these faults (Beckers et al., 2015; De Martini et al., 2004; Palyvos et al., 2010, 2007; Roberts et al., 2009), so a range of locally verified uplift:subsidence ratios (Fig. 4C) was applied to estimate their

slip rates. A comparison of geodetic rates with fault slip rate data over the last ~270 kyr broadly shows that the highest rates of deformation are in the western and central rift. However, the highest geodetic extension rates are located in the western rift whereas the highest slip rates are observed on the Lykoporia fault (7.73 +/- 0.71 mm/yr) from the central border fault system (Fig. 10). The lowest slip rates for the same period are to the east on the East/West Alkyonides faults (1.80 +/- 0.62 mm/yr), which matches low geodetic rates. The extended slip rate profile (Fig. 10B) indicates the kinematically-coherent border fault system in the central rift is much longer than presented in Figure 8, with slip rates gradually decreasing towards the Alkyonides and Aigion parts of the rift in the east and west, respectively. A slip rate low at the Aigion fault separates the central border fault system from the western border fault system in the Trizonia Basin (i.e., Psathapyrgos, Neos Erineos and Aigion faults; Fig. 10A). Fault activity maps from Ford et al. (2017) indicate that the western border fault system is younger than the central
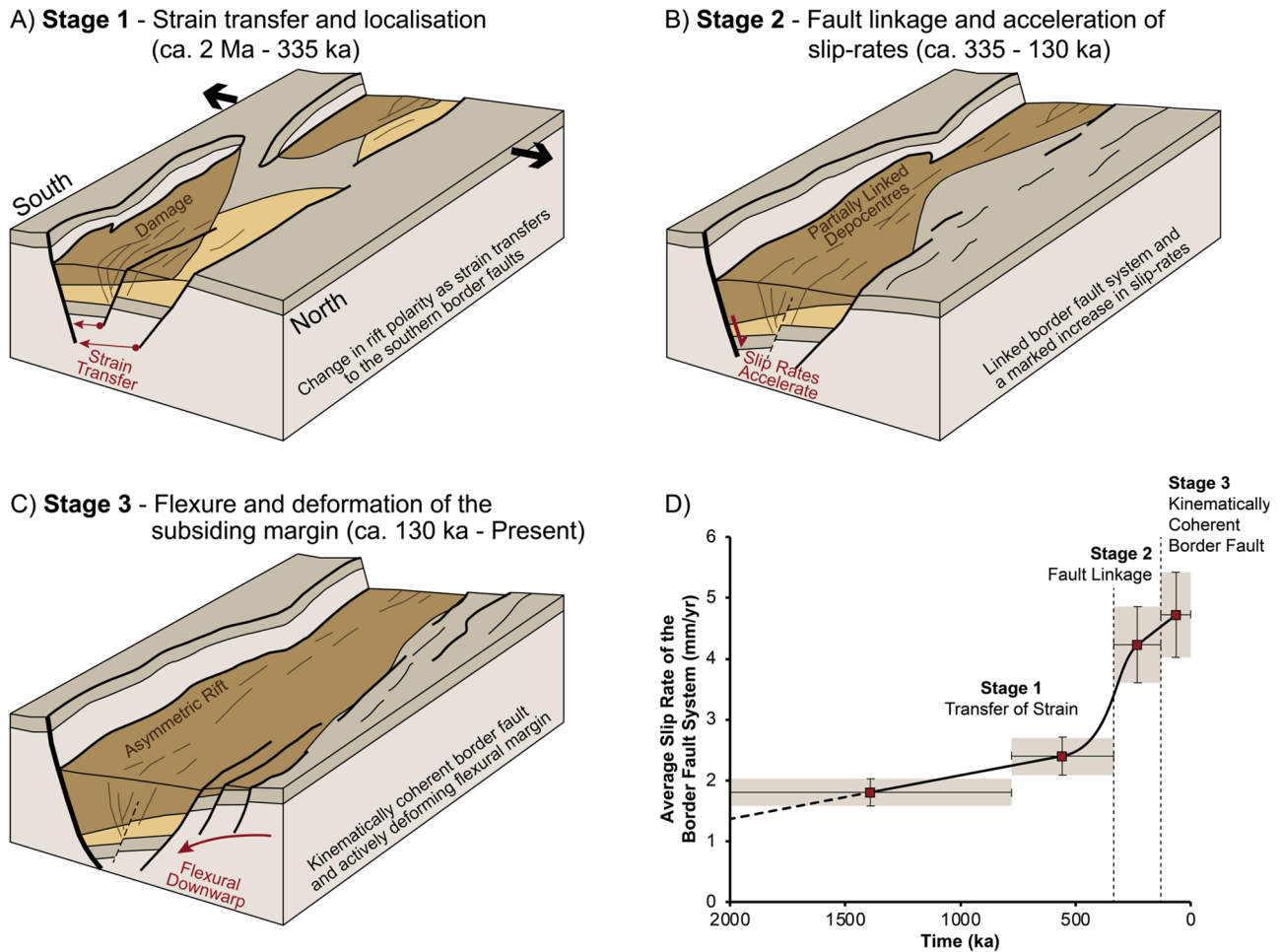
Fig 9. Cartoon illustration of border fault activity and depocentre development through time in the Gulf of Corinth. In Stage 1 (A) there is a switch in rift polarity and a transfer of strain with activity on S-dipping faults decreasing and activity on N-dipping faults increasing. In Stage 2 (B) a border fault system of major N-dipping faults becomes linked and rapidly develops higher slip rates forming an asymmetric rift. In Stage 3 (C) there is an increase in deformation on the flexural margin in response to the high slip rates on the kinematically coherent border fault system. The graph in D) summarises the average slip rates on the southern margin border fault system and how they accelerate through time. These are the averaged from the slip-rates on the Eliki, Derveni, Lykoporia, Xylokastro, Kiato and Perachora Faults shown in Figure 8. Error bars are based on the range of uplift:subsidence ratios used to estimate slip for each fault. A dip angle of 50° was applied for all faults apart from the Perachora Fault, which used a dip angle of 45°.

border fault system, with fault activity propagating to the SE over the last 400 kyr. Therefore, the slip rate low at Aigion represents an area of interaction and linkage between the western and central border fault systems. This further supports the notion that although the numerous border faults along the southern margin are segmented at the surface, they now act as a kinematically-coherent and linked fault system at depth (crustal scale) along the length of entire rift (e.g., Bell et al., 2009, 2011; Fernandez-Blanco et al., 2020).

Despite the highest long-term slip rates on the border fault system being located in the central rift, there is a sparsity of modern seismicity in this region (Fig. 10A). More seismicity is recorded in the western and eastern rift, a pattern of deformation that is confirmed by scalar seismic moment rates over the last ~50 years (Fig. 10C; see supplementary material). Moment rates over the last 50 years are lowest in the central rift, the opposite pattern to the long-term slip rates. Low moment rates over the last ~50 years also appear in the western rift, despite high geodetic rates, the M_s 6.2 1995 Aigion earthquake and related aftershocks (e.g., Bernard et al., 1997), and abundant microseismicity in the region (e.g., Lambotte et al., 2014). Furthermore, the highest moment rates over the last ~50 years are located in the eastern rift, which is at odds with both the geodetic and long-term slip rate data. This discrepancy is caused by the 1981 earthquake sequence, when several faults ruptured with a series of three M_w >6 earthquakes over a period of days

(e.g. Jackson et al., 1982). The inconsistencies between patterns of recent activity and the long-term slip rates are thought to be related to the short, decadal, timeframes of the geodetic and seismicity data that only sample strain rates from part of the seismic cycle (Bell et al., 2011), shown particularly well in the eastern part of the rift (Fig. 10). Indeed, if we estimate the seismic moment rates over the last ~320 years, we observe a spatial pattern of deformation more consistent with the long-term slip rates – highest rates in the central and western rift and lowest rates in the eastern rift (Fig. 10C). This suggests a deficit in recent fault activity in the central and western rift, at least over the last ~50 years, which has implications for assessing seismic hazard as the deficit in these parts of the rift corresponds to a M_w ~6.5 earthquake. Moreover, considering the central border fault system is clearly kinematically linked at depth, a large earthquake event in this part of the rift could rupture across multiple major fault segments, increasing the potential rupture length and magnitude.

7. Conclusions

By combining findings from the recent IODP Expedition 381 with a refined rift fault network and seismic stratigraphic framework for the offshore Corinth Rift, we have been able to examine fault activity and determine the timescales and slip rate variations associated with strain
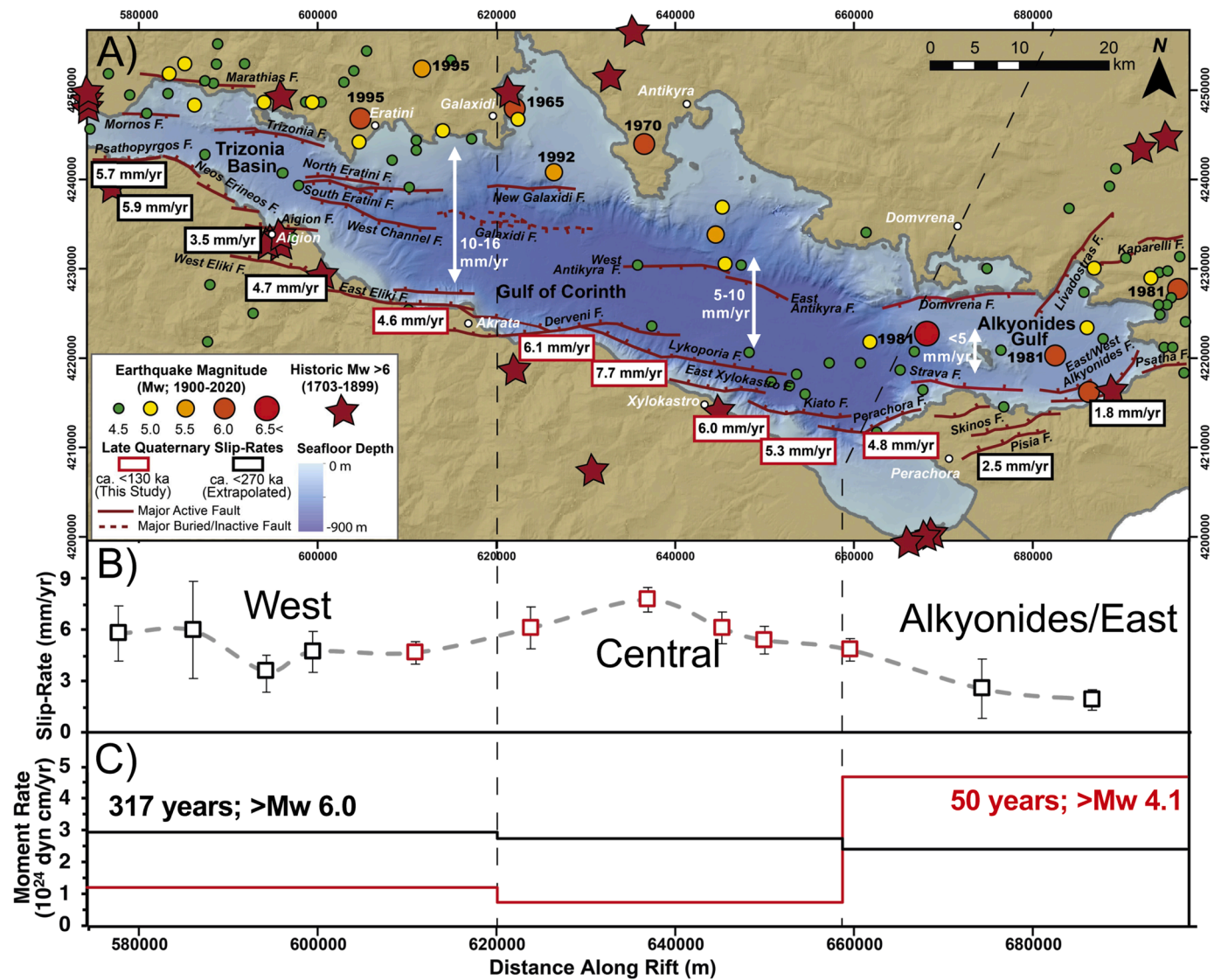
Fig 10. A) Map of major faults and fault activity including geodetic extension rates (white arrows; after Clarke et al., 1998; Briole et al., 2000; Avallone et al., 2004; Bernard et al., 2006), major earthquakes (compiled from the SHARE European earthquake catalogue and complemented with additional catalogue data from the bulletins of the National Observatory of Athens for the period 2007 – 2020). Additional information on regional historic earthquakes from Ambraseys and Jackson (1997) and Papazachos and Papazachou (2003). Late Quaternary slip-rates for the southern margin border faults over the last 270–130 kyr are also shown. B) Along-rift profile of late Quaternary slip-rates for the southern margin border fault system. Red squares are maximum slip-rates from this study that use individual uplift:subsidence ratios calculated for each fault. Black squares represent slip-rates derived from uplift:subsidence ratios applied to uplift rates averaged over similar timeframes. A ratio of 1:1.1–2.6 and fault dip of 50° were used in the Trizonia Basin, whereas a ratio of 1:1.1–4.6 and fault dip of 45° used in the Alkyonides Gulf. C) Profiles of summed moment rates for three different seismic zones that correspond with the west, central and east regions of the rift (outlined by dashed black lines). The red line is the summed moment rates for earthquakes with Mw >4.1 since 1970, whereas the black line is the summed moment rates for earthquakes with Mw >6.0 since 1703. See supplementary material for details regarding the calculation of moment rates and earthquake catalogues.

localisation and the establishment of a border fault system, precisely and at high temporal resolution. Core data from the IODP boreholes confirm the nature of glacio-eustatic cycles in the offshore sediments and provide, for the first time, the necessary absolute age constraints for seismic horizons, allowing accurate and precise quantification of fault network activity rates over timeframes of a few 100 kyr's. Our results identify three stages in the development of the central rift fault network:

1) Progressive strain localisation and transfer of strain from ~2 Ma to 130 ka characterised by decreasing activity on major S-dipping faults, increasing activity on major N-dipping faults and a change of rift polarity.

2) Linkage of the border fault system and acceleration of fault slip rates at ~335 ka, with a two-fold increase in slip rates on major N-dipping faults as they form a kinematically-linked border fault system.

3) Further increase in slip rates and rapid subsidence in the hanging wall of the now kinematically-coherent, crustal-scale border fault system at ~130 ka, resulting in increased rift margin flexure and deformation by numerous faults on the flexural margin.

These stages highlight the complex interactions that occur within a rift fault network as overall strain increases during the early stages of continental rifting. Both strain transfer and fault linkage play an important role during strain localisation and the establishment of an asymmetric rift. However, a negative feedback mechanism of this process is the subsequent deformation of the subsiding rift margin, causing

the rift deformation zone to widen and re-distribute strain. Despite this, slip rates on the border fault system have continued to increase, with some faults slipping at >7 mm/yr in the central rift since ~130 ka.

The formation of a kinematically-linked, crustal-scale fault with such high slip rates represents a significant seismic hazard in such an active rift, which is further compounded by a deficit in recent fault activity over the last 50 years in the central and western rift. Such a deficit corresponds to a M_w ~6.5 earthquake in these parts of the rift, and there is the potential to rupture several segments of the linked border fault system.

CRediT authorship contribution statement

Casey W. Nixon: . **Lisa C. McNeill:** . **Robert L. Gawthorpe:** . **Donna J. Shillington:** . **Georgios Michas:** Formal analysis, Methodology, Writing – review & editing. **Rebecca E. Bell:** . **Aaron Moyle:** Methodology, Resources. **Mary Ford:** Writing – review & editing. **Natalia V. Zakharova:** . **Jonathan M. Bull:** . **Gino de Gelder:** Data curation, Resources.

Declaration of competing interest

Data availability

Data will be made available on request.

Acknowledgements

Supplementary materials

Supplementary material associated with this article can be found, in the online version, at doi:10.1016/j.epsl.2024.118716.

References

Ambraseys, N.N., Jackson, J.A., 1997. Seismicity and strain in the gulf of Corinth (Greece) since 1694. J. Earthq. Eng. 1, 433–474. https://doi.org/10.1080/13632469708962374.

Anthonissen, D.E., Ogg, J.G., 2012. Cenozoic and Cretaceous biochronology of planktonic foraminifera and calcareous nannofossils. In: The Geologic Time Scale. Elsevier, pp. 1083–1127. https://doi.org/10.1016/b978-0-444-59425-9.15003-6.

Armijo, R., Meyer, B., King, G.C.P., Rigo, A., Papanastassiou, D., 1996. Quaternary evolution of the Corinth Rift and its implications for the Late Cenozoic evolution of the Aegean. Geophys. J. Int. 126, 11–53. https://doi.org/10.1111/j.1365-246X.1996.tb05264.x.

Avallone, A., Briole, P., Agata-Balodimou, A.M., Billiris, H., Charade, O., Mitsakaki, C., Nercessian, A., Papazissi, K., Paradissis, D., Veis, G., 2004. Analysis of eleven years of deformation measured by GPS in the Corinth Rift Laboratory area. Comptes Rendus Geosci. 336, 301–311. https://doi.org/10.1016/j.crte.2003.12.007.

Beckers, A., Hubert-Ferrari, A., Beck, C., Bodeux, S., Tripsanas, E., Sakellariou, D., De Batist, M., 2015. Active faulting at the western tip of the Gulf of Corinth, Greece, from high-resolution seismic data. Mar. Geol. 360, 55–69. https://doi.org/10.1016/j.margeo.2014.12.003.

Bell, R.E., Duclaux, G., Nixon, C.W., Gawthorpe, R.L., McNeill, L.C., 2018. High-angle, not low-angle, normal faults dominate early rift extension in the Corinth Rift, central Greece. Geology 46, 115–118. https://doi.org/10.1130/G39560.1.

Bell, R.E., McNeill, L.C., Bull, J.M., Henstock, T.J., Collier, R.E.L., Leeder, M.R., 2009. Fault architecture, basin structure and evolution of the Gulf of Corinth Rift, central Greece. Basin Res. 21, 824–855. https://doi.org/10.1111/j.1365-2117.2009.00401.x.

Bell, R.E., McNeill, L.C., Henstock, T.J., Bull, J.M., 2011. Comparing extension on multiple time and depth scales in the Corinth Rift, Central Greece. Geophys. J. Int. 186, 463–470. https://doi.org/10.1111/j.1365-246X.2011.05077.x.

Bernard, P., Briole, P., Meyer, B., Lyon-Caen, H., Gomez, J.M., Tiberi, C., Berge, C., Cattin, R., Hatzfeld, D., Lachet, C., Lebrun, B., Deschamps, A., Courboulex, F., Larroque, C., Rigo, A., Massonnet, D., Papadimitriou, P., Kassaras, J., Diagourtas, D., Makropoulos, K., Veis, G., Papazisi, E., Mitsakaki, C., Karakostas, V., Papadimitriou, E., Papanastassiou, D., Chouliaras, M., Stavrakakis, G., 1997. The Ms=6.2, June 15, 1995 Aigion earthquake (Greece): evidence for low angle normal faulting in the Corinth Rift. J. Seismol 1, 131–150. https://doi.org/10.1023/A:1009795618839.

Bernard, P., Lyon-Caen, H., Briole, P., Deschamps, A., Boudin, F., Makropoulos, K., Papadimitriou, P., Lemeille, F., Patau, G., Billiris, H., Paradissis, D., Papazissi, K., Castarède, H., Charade, O., Nercessian, A., Avallone, A., Pacchiani, F., Zahradnik, J., Sacks, S., Linde, A., 2006. Seismicity, deformation and seismic hazard in the western rift of Corinth: new insights from the Corinth Rift Laboratory (CRL). Tectonophysics 426, 7–30. https://doi.org/10.1016/j.tecto.2006.02.012.

Bosworth, W., Huchon, P., McClay, K., 2005. The Red Sea and Gulf of Aden basins. J. Afr. Earth Sci. 43, 334–378. https://doi.org/10.1016/j.jafrearsci.2005.07.020.

Briole, P., Rigo, A., Lyon-Caen, H., Ruegg, J.C., Papazissi, K., Mitsakaki, C., Balodimou, A., Veis, G., Hatzfeld, D., Deschamps, A., 2000. Active deformation of the Corinth Rift, Greece: results from repeated Global Positioning System surveys between 1990 and 1995. J. Geophys. Res. 105, 25605. https://doi.org/10.1029/2000JB900148.

Clarke, P.J., Davies, R.R., England, P.C., Parsons, B., Billiris, H., Paradissis, D., Veis, G., Cross, P.a., Denys, P.H., Ashkenazi, V., Bingley, R., Kahle, H.G., Muller, M.V., Briole, P., 1998. Crustal strain in Greece from repeated GPS measurements in the interval 1989–1997. Geophys. J. Int. 135, 195–214. https://doi.org/10.1046/j.1365-246X.1998.00633.x.

Collier, R.E.L., Dart, C.J., 1991. Neogene to Quaternary rifting, sedimentation and uplift in the Corinth Basin, Greece. J. Geol. Soc. London 148, 1049–1065. https://doi.org/10.1144/gsjgs.148.6.1049.

Cornet, F.H., Bernard, P., Moretti, I., 2004. The Corinth Rift Laboratory. Comptes Rendus Geosci 336, 235–241. https://doi.org/10.1016/j.crte.2004.02.001.

Cowie, P.A., Gupta, S., Dawers, N.H., 2000. Implications of fault array evolution for synrift depocentre development: insights from a numerical fault growth model. Basin Res. 12, 241–261. https://doi.org/10.1111/J.1365-2117.2000.00126.X.

Cowie, P.A., Roberts, G.P., Mortimer, E., 2007. Strain localization within fault arrays over timescales of 100–107 years. In: Handy, M.R., Hirth, G., Hovius, N. (Eds.), Tectonic Faults: Agents of Change on a Dynamic Earth. MIT Press, pp. 47–78.

Cowie, P.A., Underhill, J., Behn, M., Lin, J., Gill, C., 2005. Spatio-temporal evolution of strain accumulation derived from multi-scale observations of Late Jurassic rifting in the northern North Sea: a critical test of models for lithospheric extension. Earth Planet. Sci. Lett. 234, 401–419. https://doi.org/10.1016/j.epsl.2005.01.039.

de Gelder, G., Fernández-Blanco, D., Melnick, D., Duclaux, G., Bell, R.E., Jara-Muñoz, J., Armijo, R., Lacassin, R., 2019. Lithospheric flexure and rheology determined by climate cycle markers in the Corinth Rift. Sci. Rep. 9 https://doi.org/10.1038/s41598-018-36377-1.

De Martini, P.M., Pantosti, D., Palyvos, N., Lemeille, F., McNeill, L., Collier, R., 2004. Slip rates of the Aigion and Eliki Faults from uplifted marine terraces, Corinth Gulf, Greece. Comptes Rendus - Geosci. 336, 325–334. https://doi.org/10.1016/j.crte.2003.12.006.

Demoulin, A., Beckers, A., Hubert-Ferrari, A., 2015. Patterns of Quaternary uplift of the Corinth Rift southern border (N Peloponnese, Greece) revealed by fluvial landscape morphometry. Geomorphology. https://doi.org/10.1016/j.geomorph.2015.05.032.

Fernández-Blanco, D., de Gelder, G., Lacassin, R., Armijo, R., 2020. Geometry of flexural uplift by continental rifting in Corinth, Greece. Tectonics 39. https://doi.org/10.1029/2019TC005685.

Ford, M., Hemelsdaël, R., Mancini, M., Palyvos, N., 2017. Rift Migration and Lateral Propagation: Evolution of Normal Faults and Sediment-Routing Systems of the Western Corinth Rift (Greece). Geological Society Special Publication, pp. 131–168. https://doi.org/10.1144/SP439.15.

Ford, M., Rohais, S., Williams, E.A., Bourlange, S., Jousselin, D., Backert, N., Malartre, F., 2013. Tectono-sedimentary evolution of the western Corinth Rift (Central Greece). Basin Res. 25, 3–25. https://doi.org/10.1111/j.1365-2117.2012.00550.x.

Freyberg, B.von, 1973. Geologie des Isthmus von Korinth, 95. Junge Sohn, Univ. Erlangen, p. 183.

Gawthorpe, R.L., Fabregas, N., Pechlivanidou, S., Ford, M., Collier, R.E.L., Carter, G.D.O., McNeill, L.C., Shillington, D.J., 2022. Late Quaternary mud-dominated, basin-floor sedimentation of the Gulf of Corinth, Greece: implications for deep-water depositional processes and controls on syn-rift sedimentation. Basin Res. 34, 1567–1600. https://doi.org/10.1111/bre.12671.

Gawthorpe, R.L., Jackson, C.A.L., Young, M.J., Sharp, I.R., Moustafa, A.R., Leppard, C. W., 2003. Normal fault growth, displacement localisation and the evolution of normal fault populations: the Hammam Faraun fault block, Suez rift, Egypt. J. Struct. Geol. 25, 883–895. https://doi.org/10.1016/S0191-8141(02)00088-3.

Gawthorpe, R.L., Leeder, M.R., Kranis, H., Skourtsos, E., Andrews, J.E., Henstra, G.A., Mack, G.H., Muravchik, M., Turner, J.A., Stamatakis, M., 2018. Tectono-sedimentary

evolution of the Plio-Pleistocene Corinth Rift, Greece. Basin Res. 30, 448–479. https://doi.org/10.1111/bre.12260.

Goldhammer, R.K., 1997. Compaction and decompaction algorithms for sedimentary carbonates. SEPM J. Sediment. Res. 67 https://doi.org/10.1306/D42684E1-2B26-11D7-8648000102C1865D.

Hemelsdaël, R., Ford, M., 2014. Relay zone evolution: a history of repeated fault propagation and linkage, central Corinth Rift, Greece. Basin Res. 1–23. https://doi.org/10.1111/bre.12101.

Jackson, J.A., Gagnepain, J., Houseman, G., King, G.C.P., Papadimitriou, P., Soufleris, C., Virieux, J., 1982. Seismicity, normal faulting, and the geomorphological development of the Gulf of Corinth (Greece): the Corinth earthquakes of February and March 1981. Earth Planet. Sci. Lett. 57, 377–397. https://doi.org/10.1016/0012-821X(82)90158-3.

Lambotte, S., Lyon-Caen, H., Bernard, P., Deschamps, a., Patau, G., Nercessian, a., Pacchiani, F., Bourouis, S., Drilleau, M., Adamova, P., 2014. Reassessment of the rifting process in the Western Corinth Rift from relocated seismicity. Geophys. J. Int. 1822–1844. https://doi.org/10.1093/gji/ggu096.

Lavier, L.L., Buck, W.R., 2002. Half graben versus large-offset low-angle normal fault: importance of keeping cool during normal faulting. J. Geophys. Res. Solid Earth 107. https://doi.org/10.1029/2001JB000513. ETG 8-1.

Leeder, M.R., Mack, G.H., Brasier, A.T., Parrish, R.R., McIntosh, W.C., Andrews, J.E., Duermeijer, C.E., 2008. Late-Pliocene timing of Corinth (Greece) rift-margin fault migration. Earth Planet. Sci. Lett. 274, 132–141. https://doi.org/10.1016/j.epsl.2008.07.006.

Leeder, M.R., Portman, C., Andrews, J.E., Collier, R.E.L., Finch, E., Gawthorpe, R.L., McNeill, L.C., Pérez-Arlucea, M., Rowe, P., 2005. Normal faulting and crustal deformation, Alkyonides Gulf and Perachora peninsula, eastern Gulf of Corinth Rift, Greece. J. Geol. Soc. London 162, 549–561. https://doi.org/10.1144/0016-764904-075.

Maffione, M., Herrero-Bervera, E., 2022. A Relative Paleointensity (RPI)-calibrated age model for the corinth syn-rift sequence at IODP Hole M0079A (Gulf of Corinth, Greece). Front. Earth Sci. 10, 813958 https://doi.org/10.3389/feart.2022.813958.

McCartney, T., Scholz, C.A., 2016. A 1.3 million year record of synchronous faulting in the hangingwall and border fault of a half-graben in the Malawi (Nyasa) Rift. J. Struct. Geol. 91, 114–129. https://doi.org/10.1016/j.jsg.2016.08.012.

McLeod, A.E., Dawers, N.H., Underhill, J.R., 2000. The propagation and linkage of normal faults: insights from the Strathspey–Brent–Statfjord fault array, northern North Sea. Basin Res. 12, 263–284. https://doi.org/10.1111/J.1365-2117.2000.00124.X.

McNeill, L.C., Collier, R.E.L., 2004. Uplift and slip rates of the eastern Eliki fault segment, Gulf of Corinth, Greece, inferred from Holocene and Pleistocene terraces. J. Geol. Soc. London 161, 81–92. https://doi.org/10.1144/0016-764903-029.

McNeill, L.C., Collier, R.E.L., De Martini, P.M., Pantosti, D., D'Addezio, G., 2005a. Recent history of the Eastern Eliki Fault, Gulf of Corinth: geomorphology, palaeoseismology and impact on palaeoenvironments. Geophys. J. Int. 161, 154–166. https://doi.org/10.1111/j.1365-246X.2005.02559.x.

McNeill, L.C., Cotterill, C.J., Henstock, T.J., Bull, J.M., Stefatos, A., Collier, R.E.L., Papatheoderou, G., Ferentinos, G., Hicks, S.E., 2005b. Active faulting within the offshore western Gulf of Corinth, Greece: implications for models of continental rift deformation. Geology 33, 241–244. https://doi.org/10.1130/G21127.1.

Corinth active rift development. In: McNeill, L.C., Shillington, D.J., Carter, G.D.O. (Eds.), 2019a. Proceedings of the International Ocean Discovery Program. International Ocean Discovery Program. https://doi.org/10.14379/iodp.proc.381.2019.

McNeill, L.C., Shillington, D.J., Carter, G.D.O., Everest, J.D., Gawthorpe, R.L., Miller, C., Phillips, M.P., Collier, R.E.L., Cvetkoska, A., De Gelder, G., Diz, P., Doan, M.-L., Ford, M., Geraga, M., Gillespie, J., Hemelsdaël, R., Herrero-Bervera, E., Ismaiel, M., Janikian, L., Kouli, K., Le Ber, E., Li, S., Maffione, M., Mahoney, C., Machlus, M.L., Michas, G., Nixon, C.W., Oflaz, S.A., Omale, A.P., Panagiotopoulos, K., Pechlivanidou, S., Sauer, S., Seguin, J., Sergiou, S., Zakharova, N.V., Green, S., 2019b. High-resolution record reveals climate-driven environmental and sedimentary changes in an active rift. Sci. Rep. 9 https://doi.org/10.1038/s41598-019-40022-w.

Mechernich, S., Schneiderwind, S., Mason, J., Papanikolaou, I.D., Deligiannakis, G., Pallikarakis, A., Binnie, S.A., Dunai, T.J., Reicherter, K., 2018. The seismic history of the Pisia Fault (Eastern Corinth Rift, Greece) from fault plane weathering features and cosmogenic 36Cl dating. J. Geophys. Res. Solid Earth 123, 4266–4284. https://doi.org/10.1029/2017JB014600.

Moretti, I., Lykousis, V., Sakellariou, D., Reynaud, J.Y., Benziane, B., Prinzhoffer, A., 2004. Sedimentation and subsidence rate in the Gulf of Corinth: what we learn from the Marion Dufresne's long-piston coring. Comptes Rendus - Geosci. 336, 291–299. https://doi.org/10.1016/j.crte.2003.11.011.

Morley, C.K., 1999. Patterns of displacement along large normal faults: implications for basin evolution and fault propagation, based on examples from east Africa. Am. Assoc. Pet. Geol. Bull. 83, 613–634.

Morley, C.K., Vanhauwaert, P., De Batist, M., 2000. Evidence for high-frequency cyclic fault activity from high-resolution seismic reflection survey, Rukwa Rift, Tanzania. J. Geol. Soc. London. 157, 983–994. https://doi.org/10.1144/jgs.157.5.983.

Nicol, A., Walsh, J.J., Watterson, J., Underhill, J.R., 1997. Displacement rates of normal faults. Nature 390, 157–159. https://doi.org/10.1038/36548.

Nixon, C.W., Bull, J.M., Sanderson, D.J., 2014. Localized vs distributed deformation associated with the linkage history of an active normal fault, Whakatane Graben, New Zealand. J. Struct. Geol. 69, 266–280. https://doi.org/10.1016/j.jsg.2014.06.005.

Nixon, C.W., McNeill, L.C., Bull, J.M., Bell, R.E., Gawthorpe, R.L., Henstock, T.J., Christodoulou, D., Ford, M., Taylor, B., Sakellariou, D., Ferentinos, G., Papatheodorou, G., Leeder, M.R., Collier, R.E.L., Goodliffe, A.M., Sachpazi, M., Kranis, H., 2016. Rapid spatiotemporal variations in rift structure during development of the Corinth Rift, central Greece. Tectonics 35, 1225–1248. https://doi.org/10.1002/2015TC004026.

Ori, G.G., 1989. Geologic history of the extensional basin of the Gulf of Corinth (? Miocene-Pleistocene), Greece. Geology 17, 918–921. https://doi.org/10.1130/0091-7613(1989)017<0918:GHOTEB>2.3.CO;2.

Palyvos, N., Mancini, M., Sorel, D., Lemeille, F., Pantosti, D., Julia, R., Triantaphyllou, M., De Martini, P.-M., 2010. Geomorphological, stratigraphic and geochronological evidence of fast Pleistocene coastal uplift in the westernmost part of the Corinth Gulf Rift (Greece). Geol. J. 45, 78–104. https://doi.org/10.1002/gj.1171.

Palyvos, N., Pantosti, D., De Martini, P.M., Lemeille, F., Sorel, D., Pavlopoulos, K., 2005. The Aigion-Neos Erineos coastal normal fault system (western Corinth Gulf Rift, Greece): geomorphological signature, recent earthquake history, and evolution. J. Geophys. Res. Solid Earth 110, 1–15. https://doi.org/10.1029/2004JB003165.

Palyvos, N., Sorel, D., Lemeille, F., Mancini, M., Pantosti, D., Julia, R., Triantaphyllou, M., De Martini, P.M., 2007. Review and new data on uplift rates at the w termination of the Corinth Rift and the NE Rion Graben area (Achaia, NW Peloponnesos). Bull. Geol. Soc. Greece 40, 412–424. https://doi.org/10.12681/bgsg.16631.

Papazachos, V., Papazachou, K., 2003. The Earthquakes of Greece, 3rd ed. Thessaloniki, Greece.

Pechlivanidou, S., Cowie, P.A., Duclaux, G., Nixon, C.W., Gawthorpe, R.L., Salles, T., 2019. Tipping the balance: shifts in sediment production in an active rift setting. Geology 47, 259–262. https://doi.org/10.1130/G45589.1.

Richter, M.J.E.A., Brune, S., Riedl, S., Glerum, A., Neuharth, D., Strecker, M.R., 2021. Controls on asymmetric rift dynamics: numerical modeling of strain localization and fault evolution in the Kenya rift. Tectonics 40, e2020TC006553. https://doi.org/10.1029/2020TC006553.

Roberts, G.P., Houghton, S.L., Underwood, C., Papanikolaou, I., Cowie, P.A., van Calsteren, P., Wigley, T., Cooper, F.J., McArthur, J.M., 2009. Localization of Quaternary slip rates in an active rift in 10 5 years: an example from central Greece constrained by 234U- 230 Th coral dates from uplifted paleoshorelines. J. Geophys. Res. 114, B10406. https://doi.org/10.1029/2008JB005818.

Sachpazi, M., Clément, C., Laigle, M., Hirn, A., Roussos, N., 2003. Rift structure, evolution, and earthquakes in the Gulf of Corinth, from reflection seismic images. Earth Planet. Sci. Lett. 216, 243–257. https://doi.org/10.1016/S0012-821X(03)00503-X.

Sakellariou, D., Lykousis, V., Alexandri, S., Kaberi, H., Rousakis, G., Nomikou, P., Georgiou, P., Ballas, D., 2007. Faulting, seismic-stratigraphic architecture and Late Quaternary evolution of the Gulf of Alkyonides Basin-East Gulf of Corinth, Central Greece. Basin Res. 19, 273–295. https://doi.org/10.1111/j.1365-2117.2007.00322.x.

Sharp, I.R., Gawthorpe, R.L., Underhill, J.R., Gupta, S., 2000. Fault-propagation folding in extensional settings: examples of structural style and synrift sedimentary response from the Suez rift, Sinai, Egypt. Geol. Soc. Am. Bull. 112, 1877–1899. https://doi.org/10.1130/0016-7606(2000)112<1877:FPFIES>2.0.CO;2.

Shillington, D.J., Scholz, C.A., Chindandali, P.R.N., Gaherty, J.B., Accardo, N.J., Onyango, E., Ebinger, C.J., Nyblade, A.A., 2020. Controls on rift faulting in the North Basin of the Malawi (Nyasa) rift, East Africa. Tectonics 39. https://doi.org/10.1029/2019TC005633.

Skourtsos, E., Kranis, H., 2009. Structure and evolution of the western Corinth Rift, through new field data from the Northern Peloponnesus. Geol. Soc. London Spec. Publ. 321, 119–138. https://doi.org/10.1144/SP321.6.

Spratt, R.M., Lisiecki, L.E., 2016. A Late Pleistocene sea level stack. Clim. Past 12, 1079–1092. https://doi.org/10.5194/cp-12-1079-2016.

Stefatos, A., Papatheodorou, G., Ferentinos, G., Leeder, M., Collier, R., 2002. Seismic reflection imaging of active offshore faults in the Gulf of Corinth: their seismotectonic significance. Basin Res. 14, 487–502. https://doi.org/10.1046/j.1365-2117.2002.00176.x.

Taylor, B., Weiss, J.R., Goodliffe, A.M., Sachpazi, M., Laigle, M., Hirn, A., 2011. The structures, stratigraphy and evolution of the Gulf of Corinth Rift, Greece. Geophys. J. Int. 185, 1189–1219. https://doi.org/10.1111/j.1365-246X.2011.05014.x.

Taylor, S.K., Bull, J.M., Lamarche, G., Barnes, P.M., 2004. Normal fault growth and linkage in the Whakatane Graben, New Zealand, during the last 1.3 Myr. J. Geophys. Res. 109, B02408. https://doi.org/10.1029/2003JB002412.

Walsh, J.J., Childs, C., Imber, J., Manzocchi, T., Watterson, J., Nell, P.A.R., 2003. Strain localisation and population changes during fault system growth within the Inner Moray Firth, Northern North Sea. J. Struct. Geol. 25, 307–315. https://doi.org/10.1016/S0191-8141(02)00028-7.

Watkins, S.E., Whittaker, A.C., Bell, R.E., McNeill, L.C., Gawthorpe, R.L., Brooke, S.A.S., Nixon, C.W., 2018. Are landscapes buffered to high-frequency climate change? A comparison of sediment fluxes and depositional volumes in the Corinth Rift, central Greece, over the past 130 k.y. Bull. Geol. Soc. Am 131, 372–388. https://doi.org/10.1130/B31953.1.

Whitmarsh, R.B., Manatschal, G., Minshull, T.A., 2001. Evolution of magma-poor continental margins from rifting to seafloor spreading. Nature 413, 150–154. https://doi.org/10.1038/246170a0.